FULL PAPER

# Gd³⁺-Ion-Doped Upconversion Nanoprobes: Relaxivity Mechanism Probing and Sensitivity Optimization

*Feng Chen, Wenbo Bu,\* Shengjian Zhang, Jianan Liu, Wenpei Fan, Liangping Zhou, Weijun Peng, and Jianlin Shi\**

**Paramagnetic gadolinium (Gd-III)-ion-doped upconversion nanoparticles (UCNPs) are attractive optical-magnetic molecule imaging probes and are a highly promising nanoplatform for future theranostic nanomedicine design. However, the related relaxivity mechanism of this contrast agent is still not well understood and no significant breakthrough in relaxivity enhancement has been achieved. Here, the origin and optimization of both the longitudinal ($r_1$) and transverse ($r_2$) relaxivities are investigated using models of water soluble core@shell structured Gd³⁺-doped UCNPs. The longitudinal relaxivity enhancement of the nanoprobe is demonstrated to be co-contributed by inner-and outer-sphere mechanisms for ligand-free probes, and mainly by outer-sphere mechanism for silica-shielded probes. The origin of the transverse relaxivity is inferred to be mainly from an outer-sphere mechanism regardless of surface-coating, but with the $r_2$ values highly related to the surface-state. Key factors that influence the observed relaxivities and $r_2/r_1$ ratios are investigated in detail and found to be dependent on the thickness of the NaGdF$_4$ interlayer and the related surface modifications. A two orders of magnitude (105-fold) enhancement in $r_1$ relaxivity and 18-fold smaller $r_2/r_1$ ratio compared to the first reported values are achieved, providing a new perspective for magnetic resonance (MR) sensitivity optimization and multimodality biological imaging using Gd³⁺-doped UCNPs.**

## 1. Introduction

Paramagnetic gadolinium (Gd-III)-ion-doped upconversion nanoparticles (UCNPs) have attracted increasing interest as a promising bimodal molecular imaging probe because of the recent discovery of the magical roles of Gd³⁺ ions, which, after being doped in a UCNP matrix, could result in simultaneous phase/size control and upconversion luminescent efficiency enhancement,[1] fine-tuning of upconversion emission through the trapping of energy migration,[2] and more importantly, introduction of a magnetic resonance (MR) contrast imaging modality with well-preserved excellent upconversion luminescence (UCL) capabilities,[3–11] such as long luminescence lifetime,[12] improved tissue penetration depth,[13–15] minimized photodamage,[16] non-autofluorescence, and non-blinking.[4,17] Compared with traditional single modal gadolinium chelates, doping Gd³⁺ ions into the crystalline lattice of NaYF$_4$ enables an extremely high Gd³⁺-payload (over $10^4$, depending on NaGdF$_4$ thickness) and facilitates a rigid binding of the lanthanide ions, which provides additional and unique advantages for potential MR cellular imaging and, more importantly, reduced risk of toxic ion-leaching in vivo.[18,19]

According to the Solomon-Bloembergen-Morgan (SBM) theory, the paramagnetic relaxation enhancement of gadolinium chelates originates from two mechanisms: the inner-sphere (IS) and outer-sphere (OS) mechanisms.[20–22] An inner-sphere proton relaxation mechanism involves bonding of water molecules directly to Gd³⁺ ions, while no water to Gd³⁺ ion bonding is needed for an outer-sphere relaxation mechanism. The overall longitudinal relaxivity is the sum of inner-sphere relaxivity, $r_1^{IS}$, and outer-sphere relaxivity, $r_1^{OS}$ (Supporting Information Section 1). Classically, the number of coordinated water molecules ($q$) in the first coordination sphere, the mean residence time ($\tau_m$) of water molecule(s), and the rotational correlation time ($\tau_R$) are the three most structure-related parameters that have been actively studied for $r_1^{IS}$ optimization.[23] The diffusion correlation time ($\tau_D$) is a parameter that highly related to the improvement of $r_1^{OS}$. Better understanding of the dominant mechanisms and parameters that govern paramagnetic relaxation properties of given probes could lead to a greater enhancement in agent biosafety and MR sensitivity. Generally, for nanoparticle-based contrast agents, it has been well-accepted that 1) loading contrast agents (e.g., Fe$_3$O$_4$,[24] MnO,[25,26] free Gd³⁺ ions,[27] or

F. Chen, Prof. W. Bu, J. Liu, W. Fan, Prof. J. Shi
Group of Mesoporous and Low-Dimensional
Nano-materials, State Key Laboratory
of High Performance Ceramics
and Superfine Microstructure
Shanghai Institute of Ceramics
Chinese Academy of Sciences
Shanghai, 200050, People's Republic of China
E-mail: wbbu@mail.sic.ac.cn; jlshi@sunm.shcnc.ac.cn
S. Zhang, Prof. L. Zhou, Prof. W. Peng
Department of Radiology
Fudan University Shanghai Cancer Center
Department of Oncology
Shanghai Medical College
Fudan University
Shanghai 200032, China

www.MaterialsViews.com

ADVANCED
FUNCTIONAL
MATERIALS
www.afm-journal.de

FULL PAPER

gadolinium chelates[28]) into various matrixes (e.g., silica nanoparticles,[25,26,29–31] polymersome,[32] lipid,[33] fullerene,[27,28] or viral capsid[34]) could result in an altered residence time, rotational rate, and finally changed MR relaxivities; and 2) a porous matrix has been commonly reported to be a better choice than a dense one because of the relatively greater accessibility of water molecules.[25,28,30,32]

Although water soluble $Gd^{3+}$-doped UCNPs have been considered an inherently highly promising bimodal imaging nanoplatform,[7,10] attempts to promote biological imaging applications and future possible medical translation have been hindered largely by their extremely low relaxivity.[3–9] For example, the first reported longitudinal relaxivity ($r_1$) value is as low as 0.14 $mM^{-1}$ $s^{-1}$ per $Gd^{3+}$ ion.[3] Sensitivity optimization efforts have not shown significant breakthrough so far owing to the lack of understanding on the involved relaxivity mechanism. Additionally, most of previous reports have focused only on the $T_1$- by ignoring the $T_2$-contrast effect, and almost all of the reported $Gd^{3+}$-doped UCNPs have been arbitrarily defined as $T_1$-contrast agents without addressing the important $r_2/r_1$ ratios.[3–10] Here, we aim to focus on following two vital issues of water soluble $Gd^{3+}$-doped UCNP: 1) probing the possible origin of MR longitudinal and transverse contrast enhancements and 2) exploring keys to tailoring the $r_2/r_1$ ratios and dominant parameters for achieving a remarkably enhanced MR sensitivity.

## 2. Results and Discussion

We have previously demonstrated that only surface $Gd^{3+}$ ions in the ultrathin $NaGdF_4$ layer are responsible for shortening the $T_1$-relaxation time of water protons and an optimal $NaGdF_4$ thickness of ca. 1 nm has been suggested for achieving a balanced performance of both UCL and MR modalities.[7] Here, similar core@shell structured nanocrystals with a $Gd^{3+}$-free $NaYF_4$:Er/Yb (ca. 22.1 nm) core and a thin $NaGdF_4$ shell (ca. 1.2 nm) were synthesized (denoted as UCNP$_{-1}$, Supporting Information Figure S1). As-synthesized hexagonal-phase UCNP$_{-1}$ have no intrinsic aqueous solubility because of the presence of hydrophobic oleate capping ligand.[7] Shell-thickness tunable and water soluble dense (d-) and mesoporous (m-) silica layers are naturally different from each other in shell-porosity. We suppose the silica coatings could transfer UCNPs from the hydrophobic to hydrophilic, and simultaneously alter the aforementioned three critical parameters ($q$, $\tau_m$, and $\tau_R$), which creates an excellent opportunity to probe the involved relaxivity mechanisms, as well as the dominant parameters that govern the MR sensitivity (**Scheme 1**). The capability of such silica-coated UCNPs for shortening the $T_1$ and $T_2$ relaxation time of water protons is reflected by the relaxivities ($r_1$ and $r_2$), which are believed to be the result of the complex interplay between structure-related parameters, such as the coordinated-state of surface $Gd^{3+}$ ions, the thickness of $NaGdF_4$ ($t_1$), the porosity of protective silica layer, and the corresponding shell thickness ($t_2$, Scheme 1).

To demonstrate this, d- and m-$SiO_2$ coated UCNP$_{-1}$ with tunable shell-thickness were synthesized using previously reported strategies (**Figure 1**a).[35,36] The surfactant template in UCNP$_{-1}$@m-$SiO_2$ was extracted with a 1 wt% solution of NaCl in
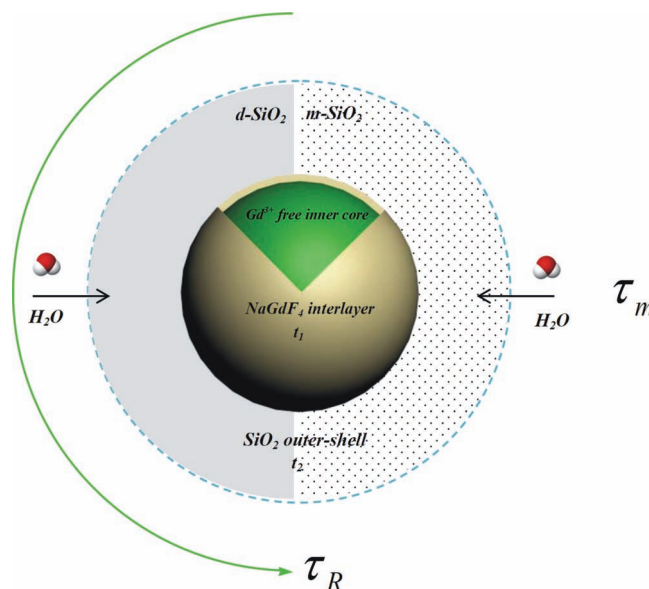


**Scheme 1.** Well-designed silica protected water soluble core@NaGdF₄ nanoprobes for investigating the MR relaxivity mechanism and sensitivity optimization. The green inner-most core stands for upconversion luminescent $Gd^{3+}$-free $NaYF_4$:Er/Yb(2/18 mol%) nanocrystals. The ultrathin interlayer $NaGdF_4$ is the MR contrast signal induced layer ($t_1$ stands for its thickness), which contains thousands of surface $Gd^{3+}$ ions as payload. Shell thickness ($t_2$) tunable dense (d-) and mesoporous (m-) silica outer layer are coated over one single particle to create difference in porosity and particle size, which could potentially alter the coordinated number of water molecules ($q$, surface $Gd^{3+}$ coordinated state dependent), the water residence time ($\tau_m$, shell-porosity dependent), and the rotational correlation time ($\tau_R$, shell-thickness dependent). Note that the sizes of the water molecules are exaggerated for clarity.

methanol.[30] As-prepared silica coated samples could all be well-dispersed in deionized water without any noticeable aggregation for days. Then, a 3.0 T human magnetic resonance imaging (MRI) scanner was employed for measuring the $r_1$ and $r_2$ relaxivities. Contrary to our prediction, for UCNP$_{-1}$@m-$SiO_2$, both the $r_1$ and $r_2$ relaxivities were virtually independent of the m-$SiO_2$ shell thickness in a range from 11.1 to 23.4 nm (Figure 1b) and kept nearly unchanged at around 4.8 $mM^{-1}$ $s^{-1}$ and 72.1 $mM^{-1}$ $s^{-1}$, respectively (Supporting Information Figure S2), while obvious increases in both $r_1$ and $r_2$ values were observed in UCNP$_{-1}$@d-$SiO_2$ (shell thicknesses ranging from 2.6 to 16.9 nm, Figure 1c, Supporting Information Figure S3). Clearly, both d- and m-$SiO_2$ shielded UCNP$_{-1}$ show remarkable $T_1$ and $T_2$-MR contrast effects (Supporting Information Figure S2,S3), with average $r_2/r_1$ ratios estimated to be 12 and 15, respectively (Supporting Information Figure S4), making them more of a $T_2$- than a $T_1$-contrast agent. Interestingly, only a slight increase in $r_1$ relaxivity has been observed when both the d- and m-$SiO_2$ shell thicknesses were approximately 11 nm (5.53 $mM^{-1}$ $s^{-1}$ versus 4.81 $mM^{-1}$ $s^{-1}$). Surprisingly, the advantage of the d-$SiO_2$ coating became much more remarkable once the thickness was greater than 15 nm (9.7 $mM^{-1}$ $s^{-1}$ versus 4.94 $mM^{-1}$ $s^{-1}$). These results suggest that water residence time (shell porosity-dependent) and the rotational correlation time (shell thickness-dependent) should not
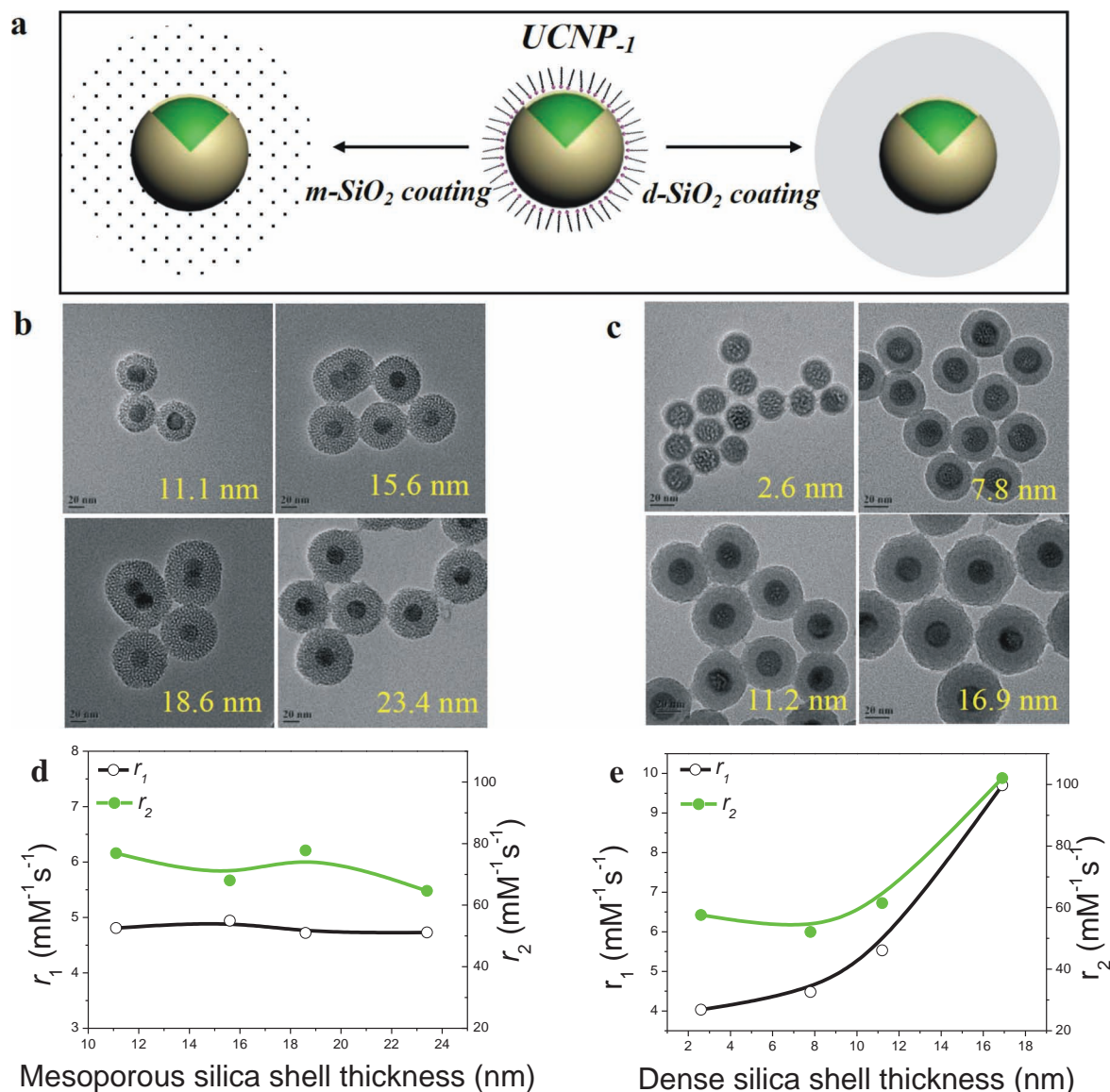
**Figure 1.** Different MR sensitivity to silica thickness changing in m- and d-silica shielded UCNP$_{-1}$. a) Schematic illustration of coating UCNP$_{-1}$ with m- and d-SiO$_2$. b) Transmission electron microscopy (TEM) images of UCNP$_{-1}$@m-SiO$_2$ with thicknesses fixed at 11.1 nm, 15.6 nm, 18.6 nm, and 23.4 nm. c) TEM images of UCNP$_{-1}$@d-SiO$_2$ with thicknesses fixed at 2.6 nm, 7.8 nm, 11.2 nm, and 16.9 nm. Scale bar 20 nm. d) Plot of $r_1$ and $r_2$ versus m-SiO$_2$ shell thickness in (d). e) Plot of $r_1$ and $r_2$ versus d-SiO$_2$ shell thickness in (c). Note: the cuves in (d,e) are drawn only as guides for the eyes.

be relaxivity limiting factors for silica shielded probes. If they were, the $r_1$ value would change significantly with the change of both shell porosity and thickness. This rules out the possible contribution from the inner-sphere mechanism.[20] Recent reports have already demonstrated that d- and m-SiO$_2$ shells possess micro- and mesopore channels, respectively, which could enable the passing through of water molecules from the exterior to interior close to the paramagnetic centers.[25,30,31,37] It is expected that the m-SiO$_2$ shell, owing to its much larger channels, is more permeable to water molecules and more useful for relaxivity enhancement.[25,30] Our observations in silica shielded UCNP$_{-1}$, however, do not follow the expectation and may indicate a quite different MR relaxivity mechanism.

To gain deeper insight into the dynamic processes involved between nanoprobes and water molecules, nuclear magnetic relaxation dispersion (NMRD) profiles of UCNP$_{-1}$@d-SiO$_2$ (shell thicknesses of 2.6 and 16.9 nm) and UCNP$_{-1}$@m-SiO$_2$ (thickness:15.6 nm) were tested over a wide range of Larmor frequencies ranging from 0.01 to 35 MHz at 310 K. To the best of our knowledge, this is the first attempt to study the field-dependent relaxivity of water-soluble Gd$^{3+}$-doped UCNP. Results show that all three profiles have a similar shape, with one relaxivity bump located at 20 MHz (UCNP$_{-1}$@d-SiO$_2$ (2.6 nm), **Figure 2**a) and the other two shifting toward higher frequency around 30 MHz (Figure 2b,c). Such relaxivity peaks are usually observed for gadolinium chelates with slow molecular motion and are
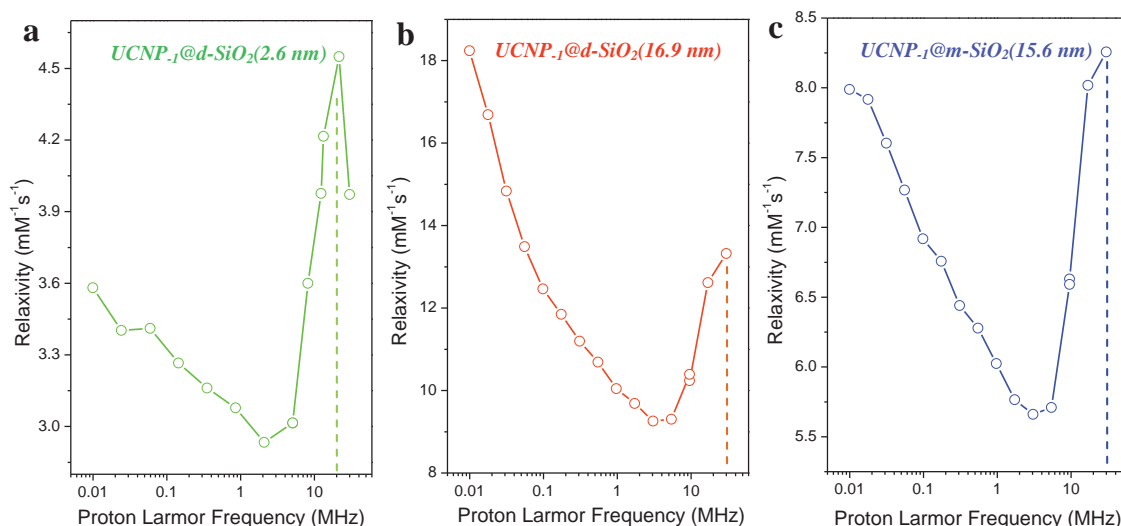
Materials
Views
www.MaterialsViews.com

ADVANCED
FUNCTIONAL
MATERIALS
www.afm-journal.de

FULL PAPER

**Figure 2.** $1/T_1$ NMRD profiles of silica-shielded UCNP$_{-1}$. a) UCNP$_{-1}$@d-SiO$_2$(2.6 nm), b) UCNP$_{-1}$@d-SiO$_2$(16.9 nm), and c) UCNP$_{-1}$@m-SiO$_2$(15.6 nm). Samples were tested with Larmor frequencies ranging from 0.01 to 30 MHz at 310 K.

indicative of the presence of a slow tumbling system that the water molecules interacting with.[20] Quick decrease rates observed between 0.01 and 1 MHz in all three profiles are quite abnormal compared with those of gadolinium chelates, making the NMRD profile fit using a standard model inapplicable.[20]

Since the direct bonding of surrounding water molecules to the surface Gd$^{3+}$ ions, which are located at the interlayer in silica shielded UCNP$_{-1}$, might not be possible, we propose that the observed longitudinal relaxivity ($r_1$) originates mainly from an outer-sphere mechanism caused by the translational diffusion of water molecules penetrating through the water permeable silica shell. Usually the higher the shell porosity, the greater the mobility of diffusion outer-sphere water molecules will be, leading to a decreased correlation diffusion time and finally reduced $r_1^{OS}$ relaxivity.[20,28] With the presence of ca. 2 nm sized mesoporous channels in the UCNP$_{-1}$@m-SiO$_2$,[38] high and nearly unaffected water mobility would be guaranteed in pore channels, even at the increased m-SiO$_2$ shell thickness, which explains the insensitivity of $r_1$-relaxivity to the m-SiO$_2$ shell-thickness in the case of UCNP$_{-1}$@m-SiO$_2$ (Figure 1d). In stark contrast, the mobility of the outer-sphere water diffusion in the dense silica shell would logically be more restricted than in mesopore channels, especially at the increased shell thickness, which results in increased correlation diffusion time and the increased $r_1^{OS}$ relaxivity (Figure 1e).[28] This inference is confirmed by the fact that UCNP$_{-1}$@m-SiO$_2$ with template CTAB (cetyl trimethylammonium bromide) kept in the mesopore channels has a higher $r_1$ relaxivity (7.17 mM$^{-1}$ s$^{-1}$, Supporting Information Figure S5) than the sample with the template being extracted (Figure 1d, average $r_1$ = 4.8 mM$^{-1}$ s$^{-1}$).

Next, we speculated that although both of the d- and m-SiO$_2$ shell could allow the diffusion of water molecules in and out, the strong coordination between adjacent silanol groups and surface Gd$^{3+}$ ions may be very likely to prevent water molecules from direct coordinating to the surface Gd$^{3+}$ ions, leading to the "quenching" of the possible contribution from an inner-sphere mechanism. To validate this, we did not coat any silica

shell on UCNP and, instead, removed the oleate capping ligand via a modified acid-treatment method to create a ligand-free UCNP$_{-1}$ (**Figure 3**a, Supporting Information Figure S6). Direct bonding of water molecules with surface lanthanide ions in ligand-free UCNP is entirely unaffected.[39] As expected, we found a much higher $r_1$ value of 10.4 mM$^{-1}$ s$^{-1}$ using the same relaxivity testing methodology (Figure 3b-left). In comparison with the $r_1$ relaxivity of UCNP$_{-1}$ coated with an ultrathin d-SiO$_2$ (shell thickness ca. 2.6 nm, $r_1$ values 4.03 mM$^{-1}$ s$^{-1}$, Supporting Information Figure S3a–c), the contribution from the co-existing inner-sphere mechanism can be verified. However, the attempt to ascertain the possible number of coordinated water molecules in ligand-free UCNP$_{-1}$ is highly challenging and the validity of defining such a value using traditional methods (most of which are only suitable for estimating $q$ value of "soft" organic gadolinium chelates but not "rigid" inorganic nanocrystals)[40–42] is still very controversial. We also noticed that, compared to UCNP$_{-1}$@d-SiO$_2$ (shell thickness ca. 2.6 nm, $r_2$ values 57.58 mM$^{-1}$ s$^{-1}$, Supporting Informatin Figure S3a–c), the $r_2$ relaxivity of ligand-free UCNP$_{-1}$ does not show the same remarkable increase as the $r_1$ value with its value estimated to be 63.16 mM$^{-1}$ s$^{-1}$ (Figure 3b-right), suggesting the absence of the inner-sphere and the dominant contribution from outer-sphere mechanism during $T_2$-contrast imaging. Moreover, the $r_2/r_1$ ratio of ligand-free UCNP$_{-1}$ is found to be 6.07 (Figure 3b), which is only half that of silica shielded samples (average $r_2/r_1$ = 12 to 15, Supporting Information Figure S4).

Clinically, a $T_1$-contrast agent ($r_2/r_1$ ratio close to 1) with high relaxivity is much more desirable than $T_2$-agent ($r_2/r_1$ > 10). For example, an intrinsic dark signal in $T_2$-weighted MRI may mislead the clinical diagnosis because lesions and tumors labeled with $T_2$-contrast agents can be confused with other hypointense areas such as bleeding, calcification, or metal deposition. The keys to tailoring the $r_2/r_1$ ratio of Gd$^{3+}$-doped UCNP are still not yet well-documented. We have shown that the silica shell coating usually leads to a $T_2$-contrast agent (Supporting Information Figure S4). Here, a larger Gd$^{3+}$-free core (>30 nm), an

ADVANCED
FUNCTIONAL
MATERIALS
www.afm-journal.de

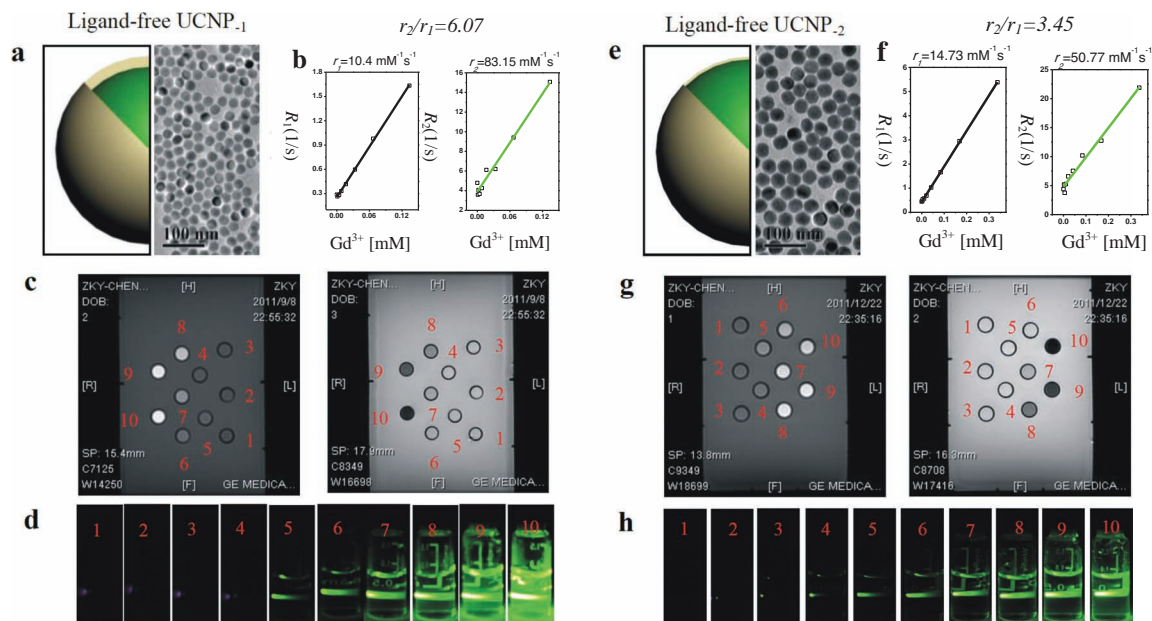Materials Views
www.MaterialsViews.com

FULL PAPER

**Figure 3.** Achieving a small $r_2/r_1$ ratio by decreasing thickness of NaGdF$_4$ in ligand-free UCNPs. a) Schematic illustration (left) and TEM image (right) of ligand-free UCNP$_{-1}$ (NaYF$_4$:Er/Yb core size $\approx$ 22.1 nm; NaGdF$_4$ thickness $\approx$ 1.2 nm). b) Corresponding plots of $R_1$ (left) and $R_2$ (right) versus Gd$^{3+}$ ions concentrations. c) Corresponding $T_1$-(left) and $T_2$-maps (right). d) Digital images of samples under excitation of NIR laser ($\lambda = 980$ nm, power = 2.0 W). e) Schematic illustration (left) and TEM image (right) of ligand-free UCNP$_{-2}$ (NaYF$_4$:Er/Yb core size $\approx$ 33.4 nm; NaGdF$_4$ thickness $\approx$ 0.9 nm). f) Corresponding plots of $R_1$ (left) and $R_2$ (right) versus Gd$^{3+}$ ions concentrations. g) Corresponding $T_1$-(left) and $T_2$-maps (right). h) Digital images of samples under excitation of NIR laser ($\lambda = 980$ nm, power = 2.0 W). The slopes in (b) and (f) indicate the $r_1$ or $r_2$ relaxivities.

ultrathin NaGdF$_4$ outer shell (<1 nm), and a ligand-free water soluble surface may be important elements for achieving a Gd$^{3+}$-doped UCNP based $T_1$-contrast ($r_2/r_1$ ratio significant lower than 10). We have demonstrated this by synthesizing new NaYF$_4$:Er/Yb@NaGdF$_4$ nanoparticles (denoted as UCNP$_{-2}$) with the diameter of NaYF$_4$:Er/Yb core fixed at 33.4 nm and NaGdF$_4$ outer shell thicknesses fixed at ca. 0.9 nm (**Figure 4**a). The thickness (or the distribution) of the NaGdF$_4$ layer over the NaYF$_4$ core has been found to be a key in influencing the observed MR relaxivity,[7,8] however, it is still a great challenge for one to ascertain the exact shell thickness (or distribution) of the NaGdF$_4$ layer due to the very close crystalline structures and compositions in core@shell structured UCNP.[2,43] All the thicknesses of NaGdF$_4$ in this study have been estimated using our previously reported method.[7] The MR relaxivity estimation shows a sharp increase of $r_1$ value from 10.4 mM$^{-1}$ s$^{-1}$ up to 14.73 mM$^{-1}$ s$^{-1}$ (Figure 3b-left and 3f-left), when the NaGdF$_4$ thickness decreases from ca. 1.2 nm to ca. 0.9 nm, in agreement with a previous report.[7] In comparison with the first reported $r_1$ value of 0.14 mM$^{-1}$ s$^{-1}$,[3] a two orders of magnitude (105-fold) enhancement in $r_1$ relaxivity has been achieved in this case. Surprisingly, we also succeeded in further decreasing the $r_2/r_1$ value to as low as 3.45 in ligand-free UCNP$_{-2}$, which is 18-fold lower than the first reported ratio ($r_2/r_1 = 62.14$)[3] and nearly 2-fold smaller than the extremely small-sized iron oxide nanoparticles (ESION, size = 3 nm, $r_2/r_1 = 6.12$).[44] The latter has recently been demonstrated to be an efficient $T_1$-contrast agent for imaging blood pool.[44] Further calculation shows that ligand-free UCNP$_{-2}$ possesses an extremely high Gd$^{3+}$ ions payload (approximately $1.55 \times 10^4$) with particle

relaxivities estimated to be $r_1 = 2.28 \times 10^5$ mM$^{-1}$ s$^{-1}$ and $r_2 = 7.87 \times 10^5$ mM$^{-1}$ s$^{-1}$ (Supporting Information Table S1), holding great potential for future UCL/MR based biological imaging, such as stem cell labeling and tracking in vivo.

Furthermore, we provide the evidence that extremely thick d-SiO$_2$ coating might represent a simple but efficient way to create an excellent $T_2$-weighted MR contrast agent ($r_2/r_1$ ratios >20). Using UCNP$_{-2}$@d-SiO$_2$ (10.8 nm) as seeds (Figure 4a), another two dense silica shielded UCNP$_{-2}$ with shell thicknesses estimated to be 19.5 and 35.3 nm, respectively, were prepared via a well-established re-growth technique (Figure 4e,i). Relaxivity study showed an obvious decrease in $r_1$ from 14.73 (ligand-free UCNP$_{-2}$, Figure 3b-left) to 9.29 mM$^{-1}$ s$^{-1}$ (UCNP$_{-2}$@d-SiO$_2$ (10.8 nm), Figure 4d-left), demonstrating the "quenching" of the inner-sphere contribution after silica-shielding once again. The $r_1$ relaxlvity shows an expected increase from 9.29 to 12.38 mM$^{-1}$ s$^{-1}$ (Figure 4d-left and h-left) as the increase of the d-SiO$_2$ shell from 10.8 to 19.5 nm, however, suffers from a quick decrease back to 9.52 mM$^{-1}$ s$^{-1}$ once the silica shell thickness increases to 35.3 nm (Figure 4l-left), suggesting an optimal shell thickness for $r_1$-relaxivity might be around 20 nm. The corresponding $r_2$ values experience a continuous increase from 88.68 to 193.05 mM$^{-1}$ s$^{-1}$ (Figure 4d-right, h-right and l-right), resulting in a remarkably enhanced $r_2/r_1$ ratio from 9.55 to 20.3.

Based on our explanation of the relaxivity mechanism, to give an in vivo UCL/MR bimodal imaging demonstration, nanocrystals with Er$^{3+}$/Tm$^{3+}$/Yb$^{3+}$ co-doped NaYF$_4$ cores and ultrathin NaGdF$_4$ shells (NaYF$_4$:Er/Tm/Yb@NaGdF$_4$, denoted as UCNP$_{-3}$, Supporting Information Figure S9a) were designed. The successful co-doping of Er$^{3+}$/Tm$^{3+}$/Yb$^{3+}$ ions has been confirmed

www.MaterialsViews.com

ADVANCED
FUNCTIONAL
MATERIALS
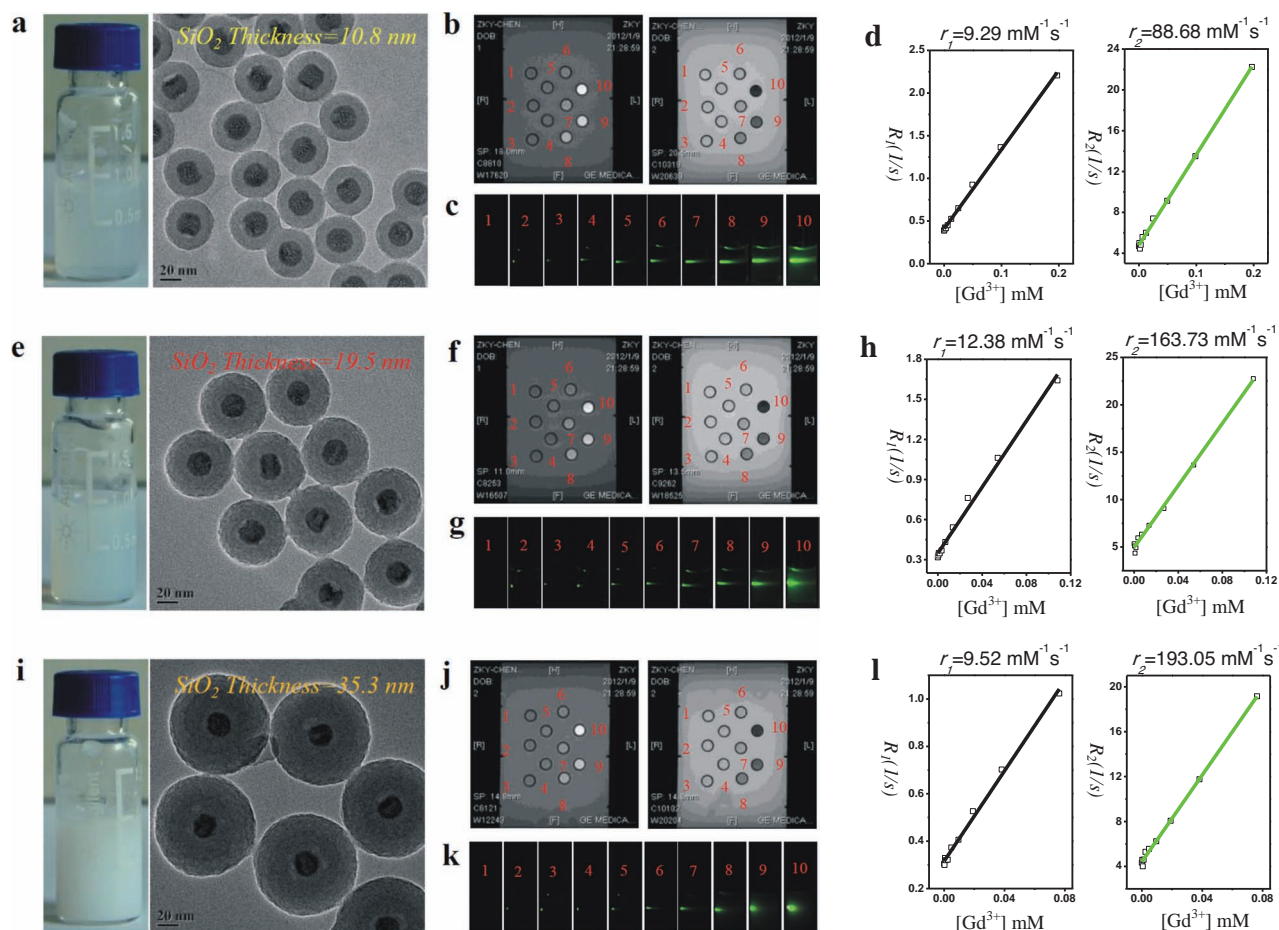www.afm-journal.de

FULL PAPER

**Figure 4.** Probing the optimal d-SiO$_2$ shell thickness and high $r_2/r_1$ ratio in water soluble UCNP$_{-2}$@d-SiO$_2$. a) Digital image (left) and TEM image of UCNP$_{-2}$@d-SiO$_2$ (10.8 nm). b) $T_1$- and $T_2$-maps of UCNP$_{-2}$@d-SiO$_2$ (10.8 nm) with varied Gd$^{3+}$ concentrations. c) Digital images of samples under excitation of NIR laser ($\lambda$ = 980 nm, power = 2.0 W). d) Plots of $R_1$ (left) and $R_2$ (right) versus Gd$^{3+}$ ions concentrations. e) Digital image (left) and TEM image of UCNP$_{-2}$@d-SiO$_2$ (19.5 nm). f) $T_1$- and $T_2$-maps of UCNP$_{-2}$@d-SiO$_2$ (19.5 nm) with varied Gd$^{3+}$ concentrations. g) Digital images of samples under excitation of a NIR laser ($\lambda$ = 980 nm, power = 2.0 W). h) Plots of $R_1$ (left) and $R_2$ (right) versus Gd$^{3+}$ ions concentrations. i) Digital image (left) and TEM image of UCNP$_{-2}$@d-SiO$_2$ (35.3 nm). j) $T_1$- and $T_2$-maps of UCNP$_{-2}$@d-SiO$_2$ (35.3 nm) with varied Gd$^{3+}$ concentrations. k) Digital images of samples under excitation of a NIR laser ($\lambda$ = 980 nm, power = 2.0 W). l) Plots of $R_1$ (left) and $R_2$ (right) versus Gd$^{3+}$ ions concentrations. The slopes indicate the $r_1$ or $r_2$ relaxivities.

by the emission bands from ultraviolet (UV, ≈350 to 370 nm ($^1D_2 \rightarrow {}^3H_6$)), visible (Vis, blue band ≈ 460 to 500 nm ($^1G_4 \rightarrow {}^3H_6$); green band ≈ 530 to 570 nm ($^4S_{3/2} \rightarrow {}^4I_{15/2}$), and red band ≈ 630 to 700 nm ($^4F_{9/2} \rightarrow {}^4I_{15/2}$)), and near-infrared (NIR, ≈770 to 810 nm ($^1G_4 \rightarrow {}^3F_4$)) regions under the NIR laser ($\lambda$ = 980 nm) excitation (Supporting Information Figure S9b and Table S2), enabling the NIR-to-vis and NIR-to-NIR small animal imaging in vivo. Ligand-free UCNP$_{-3}$ ($r_1$ = 12.5 mM$^{-1}$ s$^{-1}$, $r_2$ = 92.6 mM$^{-1}$ s$^{-1}$, $r_2/r_1$ = 7.7, Supporting Information Figure S10) was intravenously administrated (dose: 4.8 μmol Gd/kg) in SD mouse (≈170 g) and imaged in a 3.0 T MRI scanner. Clinically used Magnevist (Gd-DTPA, DTPA: diethylenetriaminepenta-cetate, Supporting Information Figure S11a) and ligand-free 8 nm sized superparamagnetic iron oxide nanoparticles (SPIONs, Supporting Information Figure S11d) were also used as control groups. Changes in the MR signal intensity (SI) in liver, one of the main probe-uptake organs,[18,45] were monitored

at timed intervals, which shows clearly enhanced (+37.9%) and reduced SI (−38.1%) values of the $T_1$- and $T_2$-models, respectively, after 30 min (**Figure 5**c,d), demonstrating the potential of the probe as a dual-weighted MR contrast agent in vivo. In contrast, Gd-DTPA and SPION could only work better in either a $T_1$- or $T_2$-model (Supporting Information Figure S11a–c and d–f). For in vivo UCL imaging, a dose of 67.4 μmol Gd/kg of probe was administrated into Kunming mouse (≈30 g) through tail veil injection. In vivo imaging was performed using a home-made UCL in vivo imaging system.[46] Excitation was provided by a continuous wave (CW) infrared laser at 980 nm and UCL signals were collected at 800 ± 12 nm and analyzed with Kodak Molecular Imaging Software. After 30 min, the whole-body UCL imaging was performed and the results show a clear signal from liver with no autofluorescence (Figure 5c, in vivo). Rapid accumulation of nanoparticles in liver and spleen have also been reported previously.[18,47] In situ and ex vivo UCL
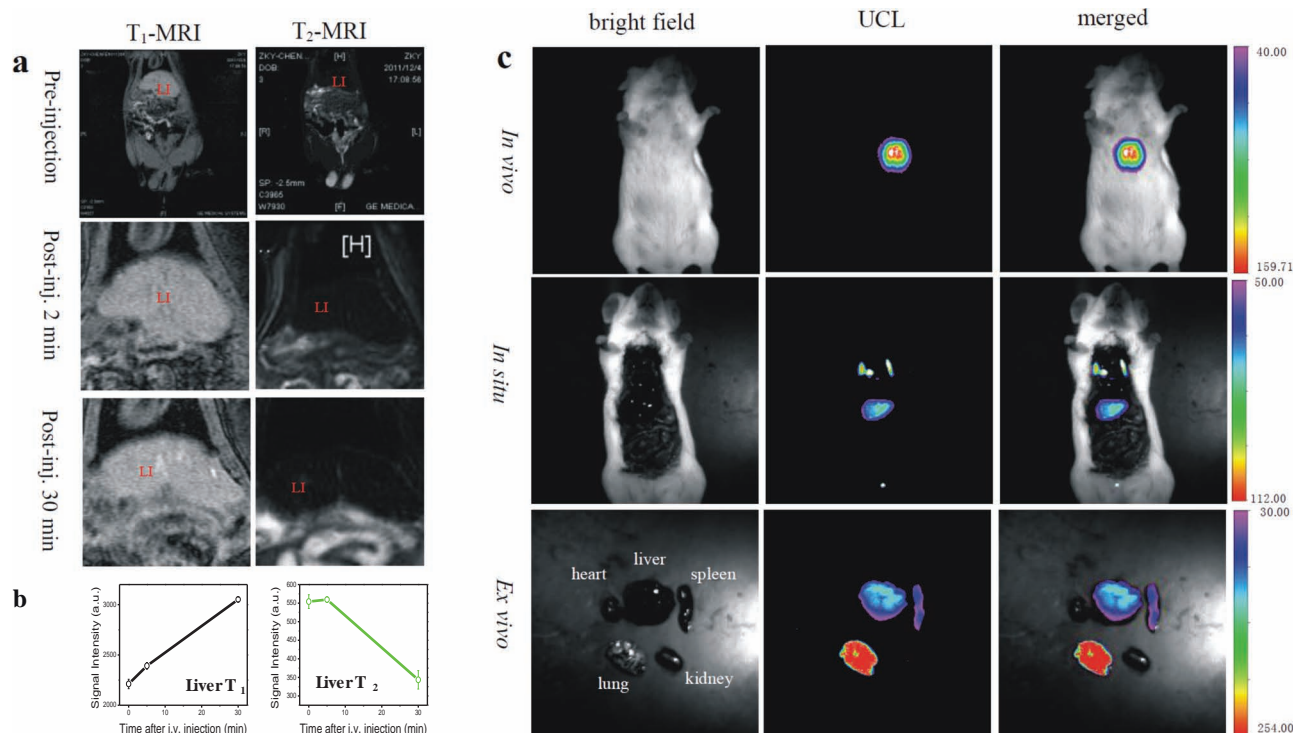
FULL PAPER



**Figure 5.** In vivo UCL/MR bimodal imaging using water-soluble ligand-free UCNP-3. a) In vivo MR $T_1$- and $T_2$-weighted images of SD mouse. Images in mouse's liver (LI) were monitored by different time points (pre-injection, post-injection 2 min, and post-injection 30 min) after i.v. injection (dose: 4.8 μmol Gd/kg). b) Plots of time-dependent signal intensity of the liver in $T_1$-model (left) and $T_2$-model (right). c) In vivo, in situ, and ex vivo upconversion luminescence imaging at 30 min post-injection of ligand-free probe-4 (dose: 67.4 μmol Gd/kg).

images further show the uptake of the probe by the spleen and lung (Figure 5c, in situ and ex vivo). These results demonstrate the great potential of the probe as an optical/magnetic dual-model imaging agent in vivo.

With the increasing attention being focused on designing inorganic-based nanoparticulate contrast agents,[48] $Gd^{3+}$-ion-doped (or containing) nanocrystals might hold great potential to solve the problems of traditional gadolinium chelates, such as single modality, low sensitivity, lack of specific targeting, possible renal dysfunction, and others.[49,50] Although previous reports have already demonstrated the capability of MR contrast enhancement effect in $Gd^{3+}$ ions containing nanocrystals,[3–10, 51–53] the reported longitudinal and transverse relaxivities have shown great variations with no reasonable explanations being provided. Probing the involved relaxivity mechanism remains an open challenge and could potentially be solved using systematic relaxivity investigations of well-selected models. Based on our previous successful demonstration of the dominant $T_1$-relaxtion time shortening effect of surface $Gd^{3+}$ ions in core@shell structured upconversion nanocrystal,[7] we attempt to address these problems by selecting d- and m-SiO$_2$ shielded NaYF$_4$:Er/Yb@NaGdF$_4$ (Scheme 1) as models by considering that silica coating is water soluble and permeable, highly biocompatible, and the porosity and thickness are easily controllable.[35,36] Using these models, contrary to our prediction, the mesoporous silica shell with higher porosity has been shown to not be very helpful for relaxivity enhancement, while

due to the dominant role of outer-sphere mechanism in silica-shielded probe, the dense silica shell has been proven to be much more useful not only for a greater relaxivity enhancement, but also potentially for a better protection of nanoprobes.

The third model, ligand-free probe, has turned out to be even more useful for mechanism probing. Because of the metal coordination between surface lanthanide ions and carboxylate,[54] the well-documented advantages of oleic acid in thermal decomposition synthesis of $Gd^{3+}$-doped UCNP are also the main cause of intrinsic aqueous non-solubility and the origin of no direct water-to-$Gd^{3+}$ coordination. Direct bonding of surrounding water molecules to the surface $Gd^{3+}$ ions would be impossible if the oleate ligand remained capped on the crystal surface or was replaced by other strongly coordinated ligands, such as silanol groups. We have confirmed this inference by comparing the relaxivity of silica-shielded and ligand-free probes, leading us to the conclusion that, as is the case for Gd-DTPA (number of coordinated water molecules is one), both the inner- and out-sphere mechanisms do co-exist in ligand-free $Gd^{3+}$-doped UCNP. This finding provides useful guidance for surface modification and further sensitivity optimization of $Gd^{3+}$-ion-doped inorganic nanocrystals. Additionally, suitable techniques for ascertaining the number of coordinated water molecules in ligand-free probes are so far unavailable, however, due to the possible difference in coordinated states of thousands of surface $Gd^{3+}$ ions, not an exact $q$ value but possibly a $q$ value distribution is more practical. Moreover, the abnormally quick decrease

rates in NMRD profiles between 0.01 and 1 MHz suggest the inapplicability of standard models for Gd$^{3+}$-doped nanocrystals during profile-fitting, highlighting the necessity for mathematic model modifications in upcoming research.

## 3. Conclusions

In conclusion, in an attempt to understand the relaxivity mechanism of water-soluble core@shell structured Gd$^{3+}$-doped UCNP, systematic investigations on well-selected models have been carried out. Inner-and outer-sphere $r_1$-relaxivity mechanisms have been demonstrated to be coexisting in ligand-free probes, while the outer-sphere mechanism has been suggested to be the main contribution to that of silica-shielded probes. The origin of $r_2$-relaxivity is inferred mainly from an outer-sphere mechanism with the $r_2$ value being surface-state related. Key factors for tuning $r_2/r_1$ ratios (ranging from ≈3 to ≈20, Supporting Information Table S3) have been found to be highly dependent on the thickness of NaGdF$_4$ interlayer and surface modifications, with the lowest ratio achieved equal to 3.45. An in vivo UCL/MR bimodal imaging using nanoprobes designed based on our mechanism probing has also been demonstrated. Our new findings provide not only deeper insight into the origin of contrast enhancements of water soluble Gd$^{3+}$-doped UCNP, but also useful strategies for achieving both high MR relaxivities and tunable $r_2/r_1$ ratios. These, we believe, will be highly favorable for enhancing and optimizing the sensitivity of other Gd$^{3+}$-ion-containing nanoparticulate probes (such as Gd$_2$O$_3$, GdPO$_4$, and GdF$_3$)[51–53] and, at the same time, speeding up the biological applications and possible medical translation of these promising optical-magnetic bimodal molecule imaging probes.

## 4. Experimental Section

*Synthesis of UCNP$_{-1}$*: First, Gd-free core, NaYF$_4$:Er(2%)/Yb(18%), was prepared. YCl$_3$·6H$_2$O (970.75 mg, 3.2 mmol), YbCl$_3$·6H$_2$O (279 mg, 0.72 mmol), ErCl$_3$·6H$_2$O (30.54 mg, 0.08 mmol) in deionized water (8 mL) were added to a 100 mL flask containing oleic acid (30 mL) and 1-octadecene (60 mL). The solution was stirred at room temperature for 1 h. The mixture was slowly heated to 120 °C under an argon atmosphere to remove water and was maintained at 160 °C for about 1 h until a homogeneous transparent yellow solution was obtained. The system was then cooled to room temperature with the flowing of argon. Then 10 mL a methanol solution of NH$_4$F (592.6 mg, 16 mmol) and NaOH (400 mg, 10 mmol) was added and the solution was stirred at room temperature for 2 h. After the methanol evaporated, the solution was heated to ≈280 to 290 °C and kept for 1.5 h, then cooled to room temperature. The resulting nanoparticles were precipitated by the addition of 40 mL ethanol and collected using centrifugation at 10 000 r/min for 10 min. The product was redispersed with 10 mL cyclohexane and precipitated by adding 30 mL ethanol, then collected by the same centrifugation. After four times washing, the final product was redispersed in 40 mL cyclohexane.

An ultrathin NaGdF$_4$ layer was grown over the Gd-free core using a seed-mediated method. GdCl$_3$·6H$_2$O (11.07 mg, 0.042 mmol) in deionized water (0.5 mL) were added to a 100 mL flask containing oleic acid (15 mL) and 1-octadecene (30 mL). The solution was stirred at room temperature for 1 h. Then the mixture was slowly heated to 120 °C under an argon atmosphere to remove water and then maintained at 160 °C for about 1 h until a homogeneous transparent yellow solution

was obtained. The system was cooled to room temperature with the flowing of argon. Then, 5 mL pre-prepared Gd-free core (dispersed in cyclohexane) was added and kept for another 30 min before heating to 80 °C to remove cyclohexane. Next, 1.25 mL methanol solution of NH$_4$F (6.241 mg, 0.169 mmol) and NaOH (4.212 mg, 0.105 mmol) was added and the solution was stirred at room temperature for 2 h. After the methanol evaporated, the solution was heated to ≈270 to 280 °C and kept for 1.5 h, before cooling to room temperature. The resulting nanoparticles were precipitated by the addition of 20 mL ethanol and then collected by centrifugation at 10 000 r/min for 10 min. The product was redispersed with 5 mL cyclohexane and precipitated by adding 15 mL ethanol, then collected by the same centrifugation. After washing four times, the final product was redispersed in 10 mL cyclohexane.

The procedures for the synthesis of UCNP$_{-2}$ and UCNP$_{-3}$ were similar to those described above, except different amounts of NaGdF$_4$ precursors (such as GdCl$_3$·6H$_2$O, NH$_4$F, and NaOH) or new lanthanide ions (such as TmCl$_3$) were added.

*Synthesis of UCNP$_{-1}$@d-SiO$_2$*: In a typical synthesis of UCNP$_{-1}$@d-SiO$_2$, Igepal CO-520 (NP-5, 1 mL) was dispersed in cyclohexane (20 mL) in a 50 mL three-necked flask and stirred for 40 min. Then, oleic acid capped UCNP$_{-1}$ in cyclohexane solution (1.5 mL, ≈100 mM) was added into the cyclohexane/NP-5 mixture and stirred for 3 h. Then ammonia (140 µL, 30%) was added dropwise, and the system was sealed and stirred for another 2 h. 200 µL tetraethyl orthosilicate (TEOS) was delivered into the system at a rate of 200 µL h$^{-1}$ using a syringe pump (WZS-50F6). The mixture was sealed and kept under magnetic stirring for 36 h at ≈18 to 22 °C before adding methanol to collect particles. The product was precipitated with excess hexane and collected by centrifugation. Then the particles were redispersed in ethanol under ultrasonic treatment, precipitated with excess hexane, and collected by centrifugation. The as-synthesized particles were washed three times using this procedure to remove excess NP-5. The as-obtained nanoparticles could be dispersed in ethanol or deioned water. For the synthesis of UCNP$_{-1}$@d-SiO$_2$ with tunable shell thickness, a different amount of TEOS was used.

*Synthesis of UCNP$_{-1}$@m-SiO$_2$*: UCNP$_{-1}$@CTAB was prepared. In a typical procedure, the UCNP$_{-1}$ in chloroform (3 mL) was added into aqueous cetyl trimethylammonium bromide (CTAB) solution (120 mL, 0.1m), and the resulting solution was sonicated using a probe-type sonicator at 600 W for 30 min to form a transparent UCNP$_{-1}$@CTAB solution. The excess amount of CTAB could be removed by decreasing the temperature to 0 °C.

The resulting solution (30 mL) was added to a mixture of water (60 mL), ethylacetate (4 mL), and NH$_4$OH solution (600 µL). The mixture was sonicated for 2 h with a 53 kHz frequency. Then TEOS (100 µL) was added dropwise and the then mixture was reacted for another 10 h. As-synthesized UCNP$_{-1}$@m-SiO$_2$ was collected by centrifugation and washed three times with ethanol to remove the unreacted species. The surfactant template was then extracted with a 1 wt% solution of NaCl in methanol. After that, the product was washed with distilled water and ethanol before being redispersed in water.

*Synthesis of Ligand-Free UCNP$_{-1}$*: In a typical synthesis, deionized water (5 mL) was added in a bottle followed by carefully adding cyclohexane-dispersed UCNP$_{-1}$ (5 mL). After that, HCl (20 µL, 1 2 M) was added before shaking the bottle for 1–2 min. Nearly all of the hydrophobic oleate-capped UCNP$_{-1}$ could be transferred to the water phase after shaking. Then, the water phase was quickly collected using separating funnel and centrifuged (13 000 r/min) for 10 min. The sample was then washed three times with acetone, resulting in ligand-free UCNP$_{-1}$. As-synthesized product could be well-dispersed in deionized water.

*NMRD Profiles*: The 1/$T_1$ NMRD profiles were measured at a number of relaxtion filed values in the 0.01–35 MHz range, using the Fast Field Cycling NMR Relaxometer produced by Stelar S.R.L. Standard pre-polarized (PP/S) and non-polarized (NP/s) acquisition sequences were used with the following parameters: temperature = 37 °C, relaxation filed = 0.01–35 MHz, acquisition field = 16.3 MHz, nucleus = 1 H, spectrometer frequency = 16.3 MHz, number of scans = 1, and 90° pulse width = 8.1 µs.

*In Vivo MR Imaging*: In vivo MR imaging of SD mouse (≈170 g) using Gd-DTPA (dose: 294 µmol Gd/kg), 8 nm sized ligand-free SPION (dose:

18.3 μmol Fe/kg), and ligand-free UCNP-3 (dose: 4.8 μmol Gd/kg) as a contrast agent was performed using a 3.0 T clinical MRI instrument. After tail vein injection, the mouse was taken for the $T_1$- and $T_2$-weighted MRI tests. The SPGR sequence was used for $T_1$-weighted MRI with the following parameters: TR/TE = 85/3.5 ms, flap angle: 80, field of view (FOV): 15 cm; matrix: 384 × 192, number of excitations (NEX): 3; slice thickness = 2 mm; space = 1 mm; and coil: QUADKNEE. The FRFSE sequence was used for $T_2$-weighted MRI test with the following parameters: TR/TE = 3720/105 ms, ETL: 16, FOV: 12 cm; matrix: 256 × 192, number of excitations (NEX): 2; slice thickness = 2 mm; space = 1 mm; and coil: QUADKNEE. All the images were then analyzed using the workstation provided by GE healthcare. Signal intensities were estimated using the eFilm Workstation.

*In Vivo Upconversion Luminescence (UCL) Imaging*: In vivo and ex-vivo UCL imaging was performed using a home-made UCL in vivo imaging system from Prof. Li's group (Advanced Materials Laboratory, Department of Chemistry, Fudan University). Images of UCL signals were analyzed with Kodak Molecular Imaging Software. Excitation was provided by the continuous wave (CW) infrared laser at 980 nm and UCL signals were collected at 800 ± 12 nm. A Kunming mouse (≈30 g) was anesthetized and tail vein injected with ligand-free UCNP-3 (dose: 67.4 μmol Gd/kg). After 30 min post-injection, the whole-body UCL imaging was performed. After that, the major organs were removed for ex vivo imaging.

*Other Characterizations*: TEM images were recorded on a JEOL 200CX microscope with an accelerating voltage of 200 kV. Standard TEM samples were prepared by dropping dilute products onto carbon-coated copper grids. The $RE^{3+}$ concentrations of samples were measured by inductively coupled plasma optical emission spectrometry (ICP-OES). Upconversion luminescence emission spectra were recorded on FluoroLog-3 Spectrofluorometer (Jobin Yvon, France), with the excitation of a 450 W xenon lamp and an external ≈0 to 1 W adjustable 980 nm semiconductor laser (Beijing Hi-tech Optoelectronic Co., China). The MR imaging experiments in water solutions were performed on a 3.0-T clinical MRI instrument (GE Signa 3.0T) and the pulse sequence used was a $T_1$-weighted FSE-XL/90 sequence with the following parameters: TR/TE = 1000, 2000, 3000, 4000/7.9 ms; FOV: 18 cm; matrix: 128 × 128; NEX: 2; slice thickness = 2 mm; space = 0.5 mm; FOV: 18 cm; and coil: QUADKNEE. Parameters for the $T_2$-weighted fast-recovery fast spin-echo (FR-FSE) sequence were as follows: TR = 4000 ms, slice thickness = 3.0, TE = 98 ms, and echo length = 15 ms. The images were then analyzed at the workstation provided by GE heathcare.

## Supporting Information

Supporting Information is available from the Wiley Online Library or from the author.

## Acknowledgements

[1] F. Wang, Y. Han, C. S. Lim, Y. Lu, J. Wang, J. Xu, H. Chen, C. Zhang, M. Hong, X. Liu, *Nature* **2010**, *463*, 1061.

[2] F. Wang, R. Deng, J. Wang, Q. Wang, Y. Han, H. Zhu, X. Chen, X. Liu, *Nat. Mater.* **2011**, *10*, 968.

[3] R. Kumar, M. Nyk, T. Y. Ohulchanskyy, C. A. Flask, P. N. Prasad, *Adv. Funct. Mater.* **2009**, *19*, 853.

[4] Y. I. Park, J. H. Kim, K. T. Lee, K. S. Jeon, H. Bin Na, J. H. Yu, H. M. Kim, N. Lee, S. H. Choi, S. I. Baik, H. Kim, S. P. Park, B. J. Park, Y. W. Kim, S. H. Lee, S. Y. Yoon, I. C. Song, W. K. Moon, Y. D. Suh, T. Hyeon, *Adv. Mater.* **2009**, *21*, 4467.

[5] H. Guo, Z. Q. Li, H. S. Qian, Y. Hu, I. N. Muhammad, *Nanotechnology* **2010**, *21*, 125602.

[6] J. Zhou, Y. Sun, X. X. Du, L. Q. Xiong, H. Hu, F. Y. Li, *Biomaterials* **2010**, *31*, 3287.

[7] F. Chen, W. Bu, S. Zhang, X. Liu, J. Liu, H. Xing, Q. Xiao, L. Zhou, W. Peng, L. Wang, J. Shi, *Adv. Funct. Mater.* **2011**, *21*, 4285.

[8] N. J. J. Johnson, W. Oakden, G. J. Stanisz, R. Scott Prosser, F. C. J. M. van Veggel, *Chem. Mater.* **2011**, *23*, 3714.

[9] J. Zhou, M. Yu, Y. Sun, X. Zhang, X. Zhu, Z. Wu, D. Wu, F. Li, *Biomaterials* **2011**, *32*, 1148.

[10] Q. Ju, D. Tu, Y. Liu, R. Li, H. Zhu, J. Chen, Z. Chen, M. Huang, X. Chen, *J. Am. Chem. Soc.* **2011**, *134*, 1323.

[11] a) M. Haase, H. Schäfer, *Angew. Chem. Int. Ed.* **2011**, *50*, 5808; b) X. Xue, F. Wang, X. Liu, *J. Mater. Chem.* **2011**, *21*, 13107; c) F. Zhang, G. B. Braun, A. Pallaoro, Y. Zhang, Y. Shi, D. Cui, M. Moskovits, D. Zhao, G. D. Stucky, *Nano Lett.* **2011**, *12*, 61; d) J. Zhou, Z. Liu, F. Y. Li, *Chem. Soc. Rev.* **2012**, *41*, 1323; e) J. Zhou, X. Zhu, M. Chen, Y. Sun, F. Li, *Biomaterials* **2012**, *33*, 6201.

[12] a) D. Tu, L. Liu, Q. Ju, Y. Liu, H. Zhu, R. Li, X. Chen, *Angew. Chem. Int. Ed.* **2011**, *50*, 6306; b) R. Deng, X. Xie, M. Vendrell, Y.-T. Chang, X. Liu, *J. Am. Chem. Soc.* **2011**, *133*, 20168.

[13] C. Wang, H. Tao, L. Cheng, Z. Liu, *Biomaterials* **2011**, *32*, 6145.

[14] D. K. Chatteriee, A. J. Rufalhah, Y. Zhang, *Biomaterials* **2008**, *29*, 937.

[15] a) Q. Liu, Y. Sun, T. Yang, W. Feng, C. Li, F. Li, *J. Am. Chem. Soc.* **2011**, *133*, 17122; b) Y. Yang, Q. Shao, R. Deng, C. Wang, X. Teng, K. Cheng, Z. Cheng, L. Huang, Z. Liu, X. Liu, B. Xing, *Angew. Chem. Int. Ed.* **2012**, *51*, 3125.

[16] S. H. Nam, Y. M. Bae, Y. I. Park, J. H. Kim, H. M. Kim, J. S. Choi, K. T. Lee, T. Hyeon, Y. D. Suh, *Angew. Chem. Int. Ed.* **2011**, *50*, 6093.

[17] S. W. Wu, G. Han, D. J. Milliron, S. Aloni, V. Altoe, D. V. Talapin, B. E. Cohen, P. J. Schuck, *Proc. Natl. Acad. Sci. USA* **2009**, *106*, 10917.

[18] L. Xiong, T. Yang, Y. Yang, C. Xu, F. Li, *Biomaterials* **2010**, *31*, 7078.

[19] Y. Liu, K. Ai, J. Liu, Q. Yuan, Y. He, L. Lu, *Angew. Chem. Int. Ed.* **2012**, *51*, 1437.

[20] P. Caravan, J. J. Ellison, T. J. McMurry, R. B. Lauffer, *Chem. Rev.* **1999**, *99*, 2293.

[21] S. Aime, M. Botta, M. Fasano, E. Terreno, *Chem. Soc. Rev.* **1998**, *27*, 19.

[22] E. J. Werner, A. Datta, C. J. Jocher, K. N. Raymond, *Angew. Chem. Int. Ed.* **2008**, *47*, 8568.

[23] L. Helm, *Future Med. Chem.* **2010**, *2*, 385.

[24] C. Paquet, H. W. de Haan, D. M. Leek, H.-Y. Lin, B. Xiang, G. Tian, A. Kell, B. Simard, *ACS Nano* **2011**, *5*, 3104.

[25] T. Kim, E. Momin, J. Choi, K. Yuan, H. Zaidi, J. Kim, M. Park, N. Lee, M. T. McMahon, A. Quinones-Hinojosa, J. W. M. Bulte, T. Hyeon, A. A. Gilad, *J. Am. Chem. Soc.* **2011**, *133*, 2955.

www.MaterialsViews.com

ADVANCED
FUNCTIONAL
MATERIALS
www.afm-journal.de

FULL PAPER

[26] Y.-K. Peng, C.-W. Lai, C.-L. Liu, H.-C. Chen, Y.-H. Hsiao, W.-L. Liu, K.-C. Tang, Y. Chi, J.-K. Hsiao, K.-E. Lim, H.-E. Liao, J.-J. Shyue, P.-T. Chou, *ACS Nano* **2011**, *5*, 4177.

[27] E. Toth, R. D. Bolskar, A. Borel, G. Gonzalez, L. Helm, A. E. Merbach, B. Sitharaman, L. J. Wilson, *J. Am. Chem. Soc.* **2005**, *127*, 799.

[28] J. S. Ananta, B. Godin, R. Sethi, L. Moriggi, X. W. Liu, R. E. Serda, R. Krishnamurthy, R. Muthupillai, R. D. Bolskar, L. Helm, M. Ferrari, L. J. Wilson, P. Decuzzi, *Nat. Nanotechnol.* **2010**, *5*, 815.

[29] J. K. Hsiao, C. P. Tsai, T. H. Chung, Y. Hung, M. Yao, H. M. Liu, C. Y. Mou, C. S. Yang, Y. C. Chen, D. M. Huang, *Small* **2008**, *4*, 1445.

[30] K. M. L. Taylor, J. S. Kim, W. J. Rieter, H. An, W. L. Lin, W. B. Lin, *J. Am. Chem. Soc.* **2008**, *130*, 2154.

[31] C. P. Tsai, Y. Hung, Y. H. Chou, D. M. Huang, J. K. Hsiao, C. Chang, Y. C. Chen, C. Y. Mou, *Small* **2008**, *4*, 186.

[32] Z. L. Cheng, D. L. J. Thorek, A. Tsourkas, *Adv. Funct. Mater.* **2009**, *19*, 3753.

[33] W. J. M. Mulder, R. Koole, R. J. Brandwijk, G. Storm, P. T. K. Chin, G. J. Strijkers, C. de Mello Donegá, K. Nicolay, A. W. Griffioen, *Nano Lett.* **2005**, *6*, 1.

[34] J. M. Hooker, A. Datta, M. Botta, K. N. Raymond, M. B. Francis, *Nano Lett.* **2007**, *7*, 2207.

[35] F. Chen, W. B. Bu, Y. Chen, Y. C. Fan, Q. J. He, M. Zhu, X. H. Liu, L. P. Zhou, S. J. Zhang, W. J. Peng, J. L. Shi, *Chem.-Asian J.* **2009**, *4*, 1809.

[36] J. Liu, W. Bu, S. Zhang, F. Chen, H. Xing, L. Pan, L. Zhou, W. Peng, J. Shi, *Chem.-Eur. J.* **2012**, *18*, 2335.

[37] Y. J. Wong, L. Zhu, W. S. Teo, Y. W. Tan, Y. Yang, C. Wang, H. Chen, *J. Am. Chem. Soc.* **2011**, *133*, 11422.

[38] J. Kim, H. S. Kim, N. Lee, T. Kim, H. Kim, T. Yu, I. C. Song, W. K. Moon, T. Hyeon, *Angew. Chem. Int. Ed.* **2008**, *47*, 8438.

[39] N. Bogdan, F. Vetrone, G. A. Ozin, J. A. Capobianco, *Nano Lett.* **2011**, *11*, 835.

[40] M. C. Alpoim, A. M. Urbano, C. F. G. C. Geraldes, J. A. Peters, *J. Chem. Soc., Dalton Trans.* **1992**, 463.

[41] A. Beeby, I. M. Clarkson, R. S. Dickins, S. Faulkner, D. Parker, L. Royle, A. S. de Sousa, J. A. Gareth Williams, M. Woods, *J. Chem. Soc., Perkin Trans.* **1999**, *2*, 493.

[42] R. M. Supkowski, W. D. Horrocks, *Inorg. Chim. Acta* **2002**, *340*, 44.

[43] K. A. Abel, J.-C. Boyer, C. M. Andrei, F. C. J. M. van Veggel, *J. Phys. Chem. Lett.* **2011**, *2*, 185.

[44] B. H. Kim, N. Lee, H. Kim, K. An, Y. I. Park, Y. Choi, K. Shin, Y. Lee, S. G. Kwon, H. B. Na, J.-G. Park, T.-Y. Ahn, Y.-W. Kim, W. K. Moon, S. H. Choi, T. Hyeon, *J. Am. Chem. Soc.* **2011**, *133*, 12624.

[45] Q. Liu, Y. Sun, C. Li, J. Zhou, C. Li, T. Yang, X. Zhang, T. Yi, D. Wu, F. Li, *ACS Nano* **2011**, *5*, 3146.

[46] L. Xiong, Z. Chen, Q. Tian, T. Cao, C. Xu, F. Li, *Anal. Chem.* **2009**, *81*, 8687.

[47] L. Cheng, K. Yang, M. W. Shao, X. H. Lu, Z. Liu, *Nanomedicine* **2011**, *6*, 1327.

[48] M. L. Matson, L. J. Wilson, *Future Med. Chem.* **2010**, *2*, 491.

[49] P. Hermann, J. Kotek, V. Kubicek, I. Lukes, *Dalton Trans.* **2008**, 3027.

[50] M. R. Prince, H. L. Zhang, J. C. Prowda, M. E. Grossman, D. N. Silvers, *Radiographics* **2009**, *29*, 1565.

[51] J. Y. Park, M. J. Baek, E. S. Choi, S. Woo, J. H. Kim, T. J. Kim, J. C. Jung, K. S. Chae, Y. Chang, G. H. Lee, *ACS Nano* **2009**, *3*, 3663.

[52] H. Hifumi, S. Yamaoka, A. Tanimoto, D. Citterio, K. Suzuki, *J. Am. Chem. Soc.* **2006**, *128*, 15090.

[53] F. Evanics, P. R. Diamente, F. van Veggel, G. J. Stanisz, R. S. Prosser, *Chem. Mater.* **2006**, *18*, 2499.

[54] L. M. Bronstein, X. L. Huang, J. Retrum, A. Schmucker, M. Pink, B. D. Stein, B. Dragnea, *Chem. Mater.* **2007**, *19*, 3624.